Author Manuscript

Author Manuscript

Author Manuscript

Author Manuscript

HHS Public Access

Author manuscript

ACS Nano. Author manuscript; available in PMC 2019 October 23.

Published in final edited form as:

ACS Nano. 2018 October 23; 12(10): 10419–10429. doi:10.1021/acsnano.8b06014.

Two-Dimensional Ti_3C_2 MXene for High-Resolution Neural Interfaces

Nicolette Driscoll[†,‡,♦], **Andrew G. Richardson**[‡,§], **Kathleen Maleski**[#,∇], **Babak Anasor**[#,∇], **Oladayo Adewole**[†,♦], **Pavel Lelyukh**[#,∇], **Lilia Escobedo**[○], **D. Kacy Cullen**[†,§,♦], **Timothy H. Lucas**[‡,§], **Yury Gogotsi**[#,∇], and **Flavia Vitale**[*,‡,‖,♦,⊥]

[†]Department of Bioengineering, University of Pennsylvania, Philadelphia, Pennsylvania 19104, United States

[‡]Center for Neuroengineering and Therapeutics, University of Pennsylvania, Philadelphia, Pennsylvania 19104, United States

[§]Department of Neurosurgery, University of Pennsylvania, Philadelphia, Pennsylvania 19104, United States

[‖]Department of Neurology, University of Pennsylvania, Philadelphia, Pennsylvania 19104, United States

[⊥]Department of Physical Medicine & Rehabilitation, University of Pennsylvania, Philadelphia, Pennsylvania 19104, United States

[#]Department of Materials Science and Engineering, Drexel University, Philadelphia, Pennsylvania 19104, United States

[∇]A.J. Drexel Nanomaterials Institute, Drexel University, Philadelphia, Pennsylvania 19104, United States

[○]School of Chemical and Biomolecular Engineering, Cornell University, Ithaca, New York 14853, United States

[♦]Center for Neurotrauma, Neurodegeneration, and Restoration, Corporal Michael J. Crescenz Veterans Affairs Medical Center, Philadelphia, Pennsylvania 19104, United States

Abstract

---

[*] **Corresponding Author** vitalef@pennmedicine.upenn.edu.

Author Contributions

N.D. and F.V. initiated the project. K.M. and P.L. prepared and characterized Ti_3C_2 MXene colloidal solutions under B.A. and Y.G. supervision. N.D. designed and fabricated Ti_3C_2 and Au electrode arrays. L.E. assisted in optimizing device fabrication protocol. N.D. performed *in vitro* electrochemical characterization and AFM imaging. B.A. performed SEM imaging. A.R. performed animal surgeries and *in vivo* electrophysiological recordings. A.R. and N.D. performed *in vivo* data analysis. O.A and D.K.C. performed cytotoxicity and immunocytochemistry assays and analyses. N.D. wrote the manuscript with contributions from all other authors. F.V. supervised the project.

Supporting Information

The Supporting Information is available free of charge on the ACS Publications website at DOI:10.1021/acsnano.8b06014.

Notes

The authors declare no competing financial interest.

Figures showing the fabrication of multichannel Ti_3C_2 neural sensors and *in vivo* noise characteristics (PDF)

Author Manuscript

Author Manuscript

Author Manuscript

Author Manuscript

High-resolution neural interfaces are essential tools for studying and modulating neural circuits underlying brain function and disease. Because electrodes are miniaturized to achieve higher spatial resolution and channel count, maintaining low impedance and high signal quality becomes a significant challenge. Nanostructured materials can address this challenge because they combine high electrical conductivity with mechanical flexibility and can interact with biological systems on a molecular scale. Unfortunately, fabricating high-resolution neural interfaces from nanostructured materials is typically expensive and time-consuming and does not scale, which precludes translation beyond the benchtop. Two-dimensional (2D) Ti_3C_2 MXene possesses a combination of remarkably high volumetric capacitance, electrical conductivity, surface functionality, and processability in aqueous dispersions distinct among carbon-based nanomaterials. Here, we present a high-throughput microfabrication process for constructing Ti_3C_2 neuroelectronic devices and demonstrate their superior impedance and *in vivo* neural recording performance in comparison with standard metal microelectrodes. Specifically, when compared to gold microelectrodes of the same size, Ti_3C_2 electrodes exhibit a 4-fold reduction in interface impedance. Furthermore, intraoperative *in vivo* recordings from the brains of anesthetized rats at multiple spatial and temporal scales demonstrate that Ti_3C_2 electrodes exhibit lower baseline noise, higher signal-to-noise ratio, and reduced susceptibility to 60 Hz interference than gold electrodes. Finally, in neuronal biocompatibility studies, neurons cultured on Ti_3C_2 are as viable as those in control cultures, and they can adhere, grow axonal processes, and form functional networks. Overall, our results indicate that Ti_3C_2 MXene microelectrodes have the potential to become a powerful platform technology for high-resolution biological interfaces.

Graphical Abstract

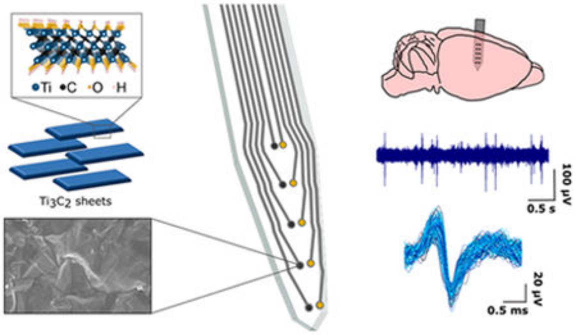

Keywords

MXene; titanium carbide; two-dimensional materials; neural interfaces; neural microelectrodes; neural recording electrodes; bioelectronics

---

Understanding the fundamental mechanisms governing the structure and function of neural circuits is critical for treating neurological disorders such as epilepsy, depression, and Parkinson's disease. Microelectrode technologies are widely used to elucidate neural dynamics on fine spatial and temporal scales (~10–100 μm and 1 ms). However, recording stable neural signals with high signal-to-noise ratio (SNR) from microscale electrodes remains a significant challenge. Current microelectrode arrays are stiff, invasive, and limited

Author Manuscript Author Manuscript Author Manuscript Author Manuscript

in their ability to provide high-fidelity long-term recordings because conventional electrode materials, including metals and silicon, are inadequate for interfacing with biological tissues. The significant mechanical mismatch between conventional electrode materials and the soft brain tissue elicits an inflammatory response that eventually results in the formation of an insulating glial scar around the implant. Additionally, as the geometric area of an electrode is decreased to approximate the size of individual neuronal processes, a corresponding rise in the electrochemical interface impedance leads to an increased susceptibility to noise sources, including thermal noise, mains interference, and signal loss to shunt pathways, which ultimately degrade signal quality. Solving these issues to achieve seamless, stable, long-term integration between man-made devices and neuronal structures requires innovation in bioelectronic materials.

One strategy commonly adopted to overcome the trade-off between electrode footprint and interface impedance is to increase the effective surface area over which ionic species in the extracellular space can interact with the electrode. This is achieved through nanopatterning, surface roughening, or electroplating with porous additives., Nanomaterials such as graphene, carbon nanotubes,, and nanowires show great promise for high-resolution neural interfaces because they offer high-specific-surface areas and desirable thermal, electronic, and mechanical properties, including flexibility and high conductivity. However, the lack of scalable assembly methods is a key barrier to their widespread adoption for neural interfaces. For example, carbon-based nanomaterials are typically hydrophobic and require the use of surfactants, superacids, or surface functionalization to allow fluid-phase assembly from aqueous dispersions. Residues from surfactants or superacids used in assembly are difficult to remove completely and can be detrimental to electrode performance or toxic to biological tissues, respectively. Surface functionalization induces defects and reduces the conductivity and strength of the resulting structures. Besides solution processing methods, chemical vapor deposition (CVD) can also be used to assemble carbon-based nanomaterials into thin films for neural electrodes. However, these processes are conducted at high temperatures that are incompatible with many flexible, biocompatible polymeric substrates and thus require tedious subsequent steps to align and transfer the films from the catalyst layer to the polymeric substrate.

MXenes are a large class of 2D nanomaterials, composed of early-transition-metal carbides, carbonitrides, and nitrides that present an exceptional combination of high electrical conductivity, strength, flexibility, and volumetric capacitance. MXenes are usually produced by selectively etching the A-group element from ternary-layered carbides of MAX phases, which have the general formula of $M_{n+1}AX_n$, where M is an early transition metal, A is a group 12–16 element of the periodic table; X is carbon, nitrogen, or both; and $n = 1, 2$, or 3. MXenes contain abundant surface-terminating functional groups, such as hydroxyl (–OH), oxygen (–O), or fluorine (–F), which endow them with a hydrophilic nature and allow flexible surface modification and functionalization. MXene hydrophilicity enables the use of high-throughput solution processing methods without the need for surfactants, superacids, or surface functionalization and may also provide an opportunity for creating functionalized platforms for drug delivery or electrochemical sensing. While MXenes have been primarily investigated for applications in energy storage,, recent studies demonstrate that MXenes hold great promise for biomedical applications, including gas and small-molecule detection,, pH

Author Manuscript Author Manuscript Author Manuscript Author Manuscript

sensing, and cancer theranostics., In the area of bioelectronics, Xu et al. recently demonstrated a single channel Ti_3C_2 MXene field-effect transistor (FET) for probing the activity of cultured neurons *in vitro*.

Of the dozens of MXenes that have been discovered, the first MXene, Ti_3C_2, has been the most extensively studied, characterized, and optimized.– Ti_3C_2 demonstrates remarkably high volumetric capacitance (1500 F/cm^3) and electronic conductivity (~10 000 S/cm). The volumetric capacitance of Ti_3C_2 exceeds that of activated graphene (~60–100 F/cm^3), carbide-derived carbons (180 F/cm^3), and graphene gel films (~260 F/cm^3). The outstanding electrical properties of Ti_3C_2, coupled with its processability and high-specific-surface area make it an extremely promising material for neural interfaces, particularly for overcoming the trade-off between geometric surface area and electrochemical interface impedance, which is a primary limitation to achieving high-fidelity recording from microscale electrodes. The high capacitance of Ti_3C_2 films is also a significant advantage for biosensing and stimulation applications, in which capacitive electrode interfaces are preferable as they avoid harmful Faradaic reactions. Finally, the hydrophilic nature of Ti_3C_2, an uncommon attribute among carbon-based nanomaterials, allows the use of simple, scalable, high-throughput solution-processing methods.

Prompted by its outstanding properties, in the present study, we investigate the suitability of Ti_3C_2 MXene for high-resolution, implantable electrodes for neural signal sensing. First, we describe a high-throughput fabrication process that combines standard photolithographic patterning with an *ad hoc* method for forming precise, micropatterned MXene films from a colloidal solution on flexible polymeric substrates. Using this custom approach, we demonstrate the feasibility of producing implantable, multichannel neural electrode arrays composed of Ti_3C_2, developing different geometries for recording both from the cortical surface and from deeper brain regions. We show that Ti_3C_2 electrodes exhibit markedly reduced impedance compared with gold (Au) electrodes of the same size and that this impedance reduction is accompanied by significant improvement in neural recording signal quality *in vivo*. In particular, when used *in vivo* for the high-fidelity recording of neural spiking activity, Ti_3C_2 electrodes show significantly improved sensitivity, reduced noise, and the ability to detect a larger number of spikes compared with Au electrodes. Finally, we demonstrate that Ti_3C_2 MXene is biocompatible with neuronal cultures and does not affect cell viability, neurite outgrowth, or synapse formation, although neurons are known to be highly sensitive to their local environment and surface interactions.

RESULTS AND DISCUSSION

Preparation and Characterization of Ti_3C_2 MXene.

We synthesized Ti_3C_2 MXene by selectively etching the aluminum atomic layers from its ternary carbide MAX-phase precursor (Ti_3AlC_2) in aqueous hydrofluoric (HF) and hydrochloric (HCl) solution for 24 h. After the performance of several steps of centrifugation and resuspension of the multilayer MXene to produce a sample of well-dispersed Ti_3C_2 flakes in deionized (DI) water, the solution could be used to spin-coat Si wafers on which devices are fabricated. The detailed Ti_3C_2 synthesis procedure is outlined in the Materials and Methods section. An overview of the process flow from Ti_3C_2

Author Manuscript

Author Manuscript

Author Manuscript

Author Manuscript

synthesis, through device fabrication, to final application in neural signal recording is shown in Figure 1A along with the atomic structure of Ti_3C_2. The atomic model shows the –OH termination for simplicity; however, the MXenes produced for this study have a distribution of –F, –OH, and –O terminations. We characterized the Ti_3C_2 MXene by scanning electron microscopy (SEM), dynamic light scattering, and UV–vis spectroscopy. SEM of Ti_3C_2 flakes deposited on a porous alumina membrane from the MXene colloidal solution reveals flake-like morphology and micrometer-scale lateral size (Figure 1B). Single-layer MXene flakes have a thickness of ~ 1 nm and lateral sizes in the range of a few hundred nanometers to a few microns, depending on the synthesis process. For application to neural electrodes, flakes with large lateral size are preferable because they produce films with higher conductivity. Thus, we disperse the Ti_3C_2 flakes in solution by manual agitation rather than sonication, as it is gentler and produces samples with larger flakes. To determine the distribution of flake sizes in our sample, we performed dynamic light scattering on a dilute Ti_3C_2 solution. The intensity distribution reveals a Z-average of 1406 ± 77 nm and a polydispersity index of 0.390, with three noticeable peaks located at 1.6 μm (81.1%), 6.8 μm (16.8%), and 164 nm (2.1%), indicating the percent intensity of different-sized flakes (Figure 1C). Finally, to confirm the composition of the Ti_3C_2 aqueous dispersion, we performed UV–vis spectroscopy from 200 to 1000 nm. The material in solution absorbed light at the characteristic UV–vis–near-infrared wavelengths for Ti_3C_2, showing hig UV absorption and a broad peak from 760 to 800 nm (Figure 1D).

Fabrication of Ti_3C_2 MXene Neural Electrode Arrays.

To evaluate the performance of Ti_3C_2 as a bioelectronic material for recording neural activity at different spatiotemporal scales, we designed two different electrode array geometries. The first electrode array is a 3 × 3 microelectrocorticography (micro-ECoG) array consisting of 50 μm × 50 μm square contacts with 300 μm pitch, covering a total recording area of 750 μm × 750 μm, for recording field potentials from the cortical surface (Figure 1E). We fabricated micro-ECoG arrays of both gold and Ti_3C_2 contacts for comparison. The second electrode array is a 10-channel laminar array with pairs of 25 μm diameter Ti_3C_2 and Au contacts arranged in a side-by-side “stereotrode” configuration (*i.e.*, close enough that each electrode in a pair could plausibly record from the same neurons) (Figure 1F). This configuration enables the recording of the spiking activity of individual neurons within deeper brain structures and allows the direct comparison of the signals recorded by the two types of electrode materials.

Unlike most carbon-based nanomaterials, the surface of Ti_3C_2 is inherently hydrophilic due to the surface terminations present, thus enabling dispersion in aqueous solution without the need for surfactants or strong acids. This property is particularly favorable for developing high-throughput microfabrication processes and patterning high-quality Ti_3C_2 films onto flexible, biocompatible polymeric substrates. To precisely and reliably micropattern Ti_3C_2 recording contacts and interconnects on flexible parylene-C substrates, we developed and optimized an *ad hoc* spin-coat and dry lift-off technique, similar to previously reported techniques for micropatterning thin films of organic polymers such as PEDOT:PSS. Briefly, we applied an antiadhesive layer to the wafer, followed by a sacrificial parylene-C layer through which patterns defined by photolithography were etched by oxygen plasma reactive ion etching (RIE). Then, we spin-coated the Ti_3C_2 colloidal solution on the wafer, thoroughly dried it, and peeled up the sacrificial parylene layer to leave Ti_3C_2 films behind only in the patterns that had been etched through the sacrificial layer. Using this technique, we were able to pattern Ti_3C_2 features with high fidelity and reproducibility. A detailed description of the fabrication procedure outlined in the Materials and Methods section, and a schematic of the procedure is shown in Figure S1.

It is worth noting that we designed the devices such that Ti_3C_2 contacts and traces overlapped with gold traces outside of the electrode array so that Ti_3C_2 was the sole material comprising the electrode contact and exclusively responsible for the device's impedance and recording performance. To provide adequate mechanical strength for precise insertion of the intracortical arrays into the brain along a straight trajectory, we manually aligned and affixed micromachined steel backings to the parylene substrate with a thin layer of polydimethylsiloxane (PDMS). Finally, for interfacing the devices with the data acquisition systems, we connected the assembled devices to custom printed circuit boards (PCBs) via zero-insertion-force (ZIF) connectors.

Characterization of Ti_3C_2 MXene Neural Electrodes.

We used electrochemical impedance spectroscopy (EIS) in a three-electrode configuration to characterize the electrochemical behavior of the electrode–electrolyte interface (Figure 2A). At the 1 kHz reference frequency, the 50 μm × 50 μm Ti_3C_2 and Au micro-ECoG electrodes show impedance values of 52 ± 25 and 206 ± 31 kΩ, respectively, while the impedance of 25 μm diameter Ti_3C_2 and Au intracortical electrodes is 219 ± 60 and 865 ± 125 kΩ, respectively (Figure 2B) (Student *t* test, $p < 0.001$). In both cases, Ti_3C_2 electrodes exhibit roughly 4-fold lower impedance than comparable Au contacts, showing an advantage in utilizing Ti_3C_2 as the active material. The Ti_3C_2 electrodes exhibit a more complex phase behavior than the Au electrodes, which display predominantly capacitive behavior (Figure 2A). It has been well-established that Ti_3C_2 exhibits mainly capacitive charge-transfer mechanisms,, and the roughness and porosity of the film contributes to its behavior as a nonideal capacitor, as shown by the higher values of the impedance phase. Furthermore, the functional groups on the surface of the Ti_3C_2 flakes can interact with the ionic species in the electrolyte, possibly leading to mixed-charge-transfer mechanisms.

One attribute that can reduce electrode impedance is the overall surface roughness or porosity, which produces an increase in the effective surface area without impacting the device footprint. We evaluated the surface morphology of the Ti_3C_2 electrodes with SEM and atomic force microscopy (AFM) and found that the electrode surface is composed of a dense network of overlapping Ti_3C_2 flakes (Figure 2C) of nanoscale thickness and several micrometers in lateral size. AFM mapping of the surface further elucidates the rough and wrinkled morphology and reveals an average surface roughness of 32 nm (Figure 2D). The thickness of the Ti_3C_2 films forming the electrodes, as measured by a profilometer following lift-off patterning, is 200 ± 30 nm. The rough surface morphology we observe suggests that ions can interact with the Ti_3C_2 electrodes over a large effective surface area, likely contributing to their remarkably low impedance compared with metal electrodes.

Author Manuscript Author Manuscript Author Manuscript Author Manuscript

Author Manuscript Author Manuscript Author Manuscript Author Manuscript

In Vivo Neural Signal Recording.

To assess the functionality of Ti_3C_2 neural electrodes *in vivo*, we performed acute recording experiments in rats under ketamine-dexmede-tomidine anesthesia. Schematic of the recording setup for both the brain surface (micro-ECoG) and the brain-penetrating (intracortical) arrays are shown in Figure 3A. First, we tested Ti_3C_2 and Au micro-ECoG devices placed over sensorimotor cortex (Figure 3A, left). On both electrodes, we detected clear physiological signals (Figure 3B). However, the background noise level in the spike band (500–5000 Hz) was lower in the Ti_3C_2 recordings than in the Au recordings: 3.7 ± 0.3 versus 6.6 ± 2.0 μVrms, respectively. The power spectral density (PSD) of the recorded signals confirmed the presence of two brain rhythms commonly observed in rats under this type of anesthesia: slow oscillations at 1–2 Hz and γ oscillations at 40–70 Hz (Figure 3C). These two rhythms were, in fact, coupled, as revealed by computing the signal average in a window centered on gamma oscillation events (Figure 3D). The γ bursts occurred on average at a specific phase, namely the peak, of the slow oscillation, as reported previously with traditional metal electrode recordings.’ Thus, the Ti_3C_2 electrode surface recordings reproduced known physiology in this brain state and with lower noise than Au electrodes.

Next, we inserted electrode arrays intracortically to record neuronal action potentials (spikes). The 10-channel intracortical arrays were composed of both Ti_3C_2 and Au electrodes (Figure 3A, right). Examples of the neural activity recorded from a Ti_3C_2 contact are shown in Figure 3E,F. The neuron recorded on this Ti_3C_2 electrode tended to fire rhythmically at a low frequency (<5 Hz) but with bursts of spikes in each cycle (Figure 3E,G). The full bandwidth recording revealed that the rhythmic spiking of this cell was related to the slow oscillation in the field potential (Figure 3H). As with γ oscillations recorded at the brain surface, spikes from this neuron were biased to occur at a particular phase of the rhythm (Figure 3I), which again had a frequency of 1–2 Hz (Figure 3J). Although these results demonstrate the functionality of intracortical Ti_3C_2 electrodes, we next pursued the more critical question of how they perform relative to the Au electrodes.

The intracortical array was designed such that each pair of Ti_3C_2 and Au electrodes was arranged as a stereotrode, with contacts separated by 35 μm. This configuration allows the direct comparison of the signal recorded with the two types of electrodes at different depths in the sensorimotor cortex (Figure 4A). Spiking activity was observed predominantly on the distal three pairs of electrodes (Figure 4B). Spikes that occurred simultaneously on adjacent Ti_3C_2 and Au electrodes in a pair were considered to be generated by the same neuron. For each of these “common spikes,” we computed the SNR from each electrode. The mean of the distribution of $SNR_{MXene} - SNR_{Au}$ was, at all three depths, greater than zero (permutation test, $p < 0.001$), indicating that spikes recorded on the Ti_3C_2 electrodes had higher SNR than those on the Au electrodes (Figure 4C). Additionally, Ti_3C_2 electrodes recorded more “unique spikes”, spikes that occurred only on one electrode in the pair (Figure 4D). These unique spikes had lower amplitudes than the common spikes and therefore may have arisen from neurons located further from the electrode sites. This result suggests that, due to their lower impedance, the Ti_3C_2 electrodes have a larger “seeing distance”, allowing them to resolve spiking activity from a larger volume of tissue.

Author Manuscript Author Manuscript Author Manuscript Author Manuscript

Finally, we quantified the power spectrum of the wideband neural signal recorded on representative Ti_3C_2 and Au electrodes in the array (Figure S2). The Ti_3C_2 electrode recorded higher overall power across a wide range of frequencies. Additionally, a significant peak at 60 Hz was observed on the Au electrode, while this peak is completely absent on the adjacent Ti_3C_2 contact, which indicates that the higher impedance Au electrodes are more susceptible to mains interference.

Ti_3C_2 MXene Neuronal Biocompatibility.

MXenes have shown great promise in a number of biomedical applications including cancer theranostics, diagnostic imaging, and biosensing. Recent studies report that MXenes are biocompatible to immortalized tumor cell lines *in vitro* and at the systemic level when injected intravenously *in vivo*., However, very little is known about the safety and compatibility of MXenes to neuronal cells. Thus, we performed cytotoxicity studies *in vitro* on primary cortical neurons grown on Ti_3C_2 films. At 7 days *in vitro* (DIV), quantification of the percent viable neurons showed no significant difference in cell survival between Ti_3C_2 and control polystyrene cultures (Ti_3C_2: 84.4 ± 4.40%, polystyrene: 87.3 ± 2.05%; $p > 0.64$) (Figure 5A–C). Cell densities on Ti_3C_2 at 7 DIV were significantly sparser than those on polystyrene (Ti_3C_2: 650 ± 155 neurons per square millimeter, polystyrene: 1132 ± 132 neurons per square millimeter; $p < 0.05$), suggesting that additional surface treatments may be required to promote neuronal adhesion. Although there was also a reduction in overall neurite density on the Ti_3C_2 cultures, there were no significant differences in neurite outgrowth per neuron (Ti_3C_2: 5.73 ± 1.05 neurites per neuron, polystyrene: 6.00 ± 0.737 neurites per neuron; $p > 0.8$). Immunocytochemistry revealed widespread network formation on both substrates (Figure 5D-I), with neurons extending branching neurites (Figure 5E,H) and synapsin-positive puncta present surrounding cell bodies and at axon–soma junctions (Figure 5F,I).

Overall, neurons reproducibly adhered, grew, and formed neuronal networks on both Ti_3C_2 and polystyrene, with both substrates yielding equivalent neuronal viability and neurite outgrowth per neuron out to at least 7 DIV. These results indicate that Ti_3C_2 is capable of supporting neuronal growth and network formation with negligible cytotoxicity relative to established cell culture substrates. While both cultures exhibited similar neurite counts per neuron and axonal and synaptic presence at 7 DIV, Ti_3C_2 cultures had a reduction in both neuron density and a commensurate reduction in neurite outgrowth compared to polystyrene. These results suggest decreased neuronal adhesion on Ti_3C_2 compared to polystyrene, which indicates further optimization of the pretreatment protocol used to culture neurons and promote neuronal adhesion and neurite growth on Ti_3C_2 films is necessary.

CONCLUSIONS

In this study, we developed a protocol for fabricating high-resolution Ti_3C_2 MXene neural electrode arrays using simple, scalable solution-processing methods. The methodology described here can easily be extended to create other types of MXene sensors, and the extraordinary processability of MXenes highlights the potential for cost-effective production of MXene biosensors at industrial scales, which is not currently possible for devices based

Author Manuscript

Author Manuscript

Author Manuscript

Author Manuscript

on other carbon nanomaterials. The high conductivity of Ti_3C_2, coupled with the high effective surface area of MXene films, endows Ti_3C_2 neural electrodes with remarkably low impedance, which improves their sensitivity for recording neural activity at fine spatial scales. Recordings from Ti_3C_2 micro-ECoG devices showed known physiologic signatures with lower baseline noise than control Au electrodes. Using high-resolution intracortical arrays, we demonstrated that Ti_3C_2 electrodes record multiunit neuronal spiking activity with improved SNR compared with gold electrodes. Additionally, our observation that Ti_3C_2 electrodes recorded overall a larger number of spikes, many of which were low-amplitude, suggests that these electrodes are capable of recording from a larger volume of brain tissue. Thus, Ti_3C_2 microelectrodes may represent a significant advance for the sensitive detection of neuronal spiking activity compared with conventional silicon- or metal-based microelectrodes. Furthermore, our observations suggest that Ti_3C_2 could be useful for a range of implantable sensors beyond neural recording applications, such as cardiac monitoring, and it may be a candidate for the replacement of expensive electrode materials, such as platinum, currently used in many implantable devices. Finally, although the biocompatibility of Ti_3C_2 has been demonstrated following systemic injection for cancer theranostic applications, the compatibility of this material to neurons and brain cells has so far remained largely untested. Our work shows that not only do neurons remain viable in contact with Ti_3C_2 but they also extend neurites and form functional networks when cultured on Ti_3C_2 films. While more work needs to be done, our experiments indicate that Ti_3C_2, and possibly other MXenes, have significant potential to transform the field of implantable sensors in both research and clinical applications. The promising bioelectronic properties and versatility in fabrication of Ti_3C_2 MXene may both reduce cost and improve performance in current and future medical devices.

MATERIALS AND METHODS

Preparation of Ti_3C_2 Colloidal Solution.

Ti_3AlC_2 MAX-phase carbide powder synthesis has been explained elsewhere. A total of 5 g of Ti_3AlC_2 was added slowly to a chemical etchant [50 mL, 12 M HCl (Alfa Aesar), deionized (DI) water, 49% HF (Sigma-Aldrich), 6:3:1 ratio] while it was in an ice bath and was agitated on a stir plate (24 h, 500 rpm, 25 °C, Teflon stir bar) in an unsealed container to make multilayer Ti_3C_2 MXene (ML-MXene). The solution was then centrifuged (2 min, 3500 rpm, ~6 cycles) in 2 large tubes (175 mL) to reach ~6 pH. An intercalant was used to delaminate Ti_3C_2 into single flakes by mixing 10 g of lithium chloride (LiCl, Alfa Aesar) and 100 mL of DI water in an ice bath 30 min prior to adding the ML-MXene. After the addition of Ti_3C_2, the solution was manually shaken until small bubbles appeared on the side of the container (~15 min), and the solution was stirred on a stir plate (at least 4 h at 300 rpm). The solution was then centrifuged (3500 rpm, 2 cycles, 2 min) in 2 large tubes to cause the sediment to swell. Next, the sediment was evenly dispersed and centrifuged (3500 rpm, 1 h, 2 cycles) in 4 150 mL tubes, Finally, to remove insoluble contaminates from the single flake and ML-MXene, the sediment was dispersed (10 min of manual shaking) in 300 mL of DI water in 2 150 mL tubes and centrifuged (500 rpm, 2 min). The resulting supernatant was centrifuged at 10000 rpm for 15 min in 6 small tubes (50 mL), and the sediment (with concentration of 10 mg/mL) was collected. Prior to spin-coating, the Ti_3C_2

solution was dispersed for centrifugation (3500 rpm, 2 min) in 2 small tubes, and the supernatant was collected to be used for spincoating. The concentration of Ti_3C_2 in the supernatant was measured (~10 mg/mL) by vacuum filtration of the solution (1 mL) on a hydrophobic Celgard membrane.

Characterization of Ti_3C_2 Flakes.

As-prepared Ti_3C_2 was characterized by SEM, dynamic light scattering, and UV–vis spectroscopy. SEM was performed using a Zeiss Supra 50 VP (Zeiss, Germany) at an accelerating voltage of 5 kV by vacuum filtering a dilute (~0.01 mg/mL) solution over a porous alumina membrane (Anodisc, 0.1 μm pore size, Whatman). Dynamic light scattering was performed using a dilute Ti_3C_2 solution (<0.1 mg/mL) in a polystyrene disposable cuvette (Malvern Instruments, Zetasizer, NanoZS). The measurement was repeated 5 times, and an average was reported (Figure 1C). UV–vis spectroscopy was conducted from 200 to 1000 nm on a Ti_3C_2 solution diluted 1000× (ThermoScientific Evolution 201).

Device Fabrication and Assembly.

A silicon wafer was coated with a 4 μm thick layer of parylene-C. Metal traces and pads (Ti/Au = 10:100 nm) were patterned using standard photolithography and lift-off processes. The wafer was coated with an anti-adhesive layer (1% Micro-90), and then a second, 3 μm thick sacrificial layer of parylene-C was deposited. Patterns for MXene traces and electrode contacts were defined by photolithography with the negative resist NR71-3000p and subsequent oxygen plasma reactive-ion etching (RIE) to etch through the sacrificial parylene-C layer. A Ti_3C_2 colloidal solution was spin-coated on the wafer, and the wafer was subsequently baked at 130 °C for 3 h to ensure that the resulting Ti_3C_2 film was fully dried. A 50 nm thick layer of SiO_2 was deposited by electron-beam evaporation to serve as a protective mask on the Ti_3C_2 patterns during subsequent fabrication steps. The sacrificial parylene-C layer was then manually peeled up with tweezers, leaving behind Ti_3C_2/SiO_2 only on the Ti_3C_2 contacts and traces that were previously defined. After the deposition of a top 4 μm thick parylene-C encapsulation layer, an etch mask was defined through photolithography, electron-beam deposition of aluminum (100 nm), and lift-off to define the outline of the devices and openings over Au bonding pads and electrode contacts. The exposed parylene-C was etched with oxygen RIE, and the Al etch mask was subsequently removed via wet etching. The SiO_2 protective layer covering the Ti_3C_2 contacts was etched with 1:6 buffered oxide etchant (BOE: 6 parts 40% NH_4F, 1 part 49% HF, Sigma-Aldrich) to expose the Ti_3C_2 electrode sites. Finally, the completed devices were released from the silicon wafer. Both micro-ECoG and intracortical electrode arrays were fabricated using this procedure, with different photomasks to define the geometries. Steel backings (2.5 μm thick) were laser-micromachined (IPG IX280-DXF Green Laser Micromachining, 532 nm) to provide mechanical support for insertion of the intracortical arrays. Devices were carefully aligned and manually fixed to these steel backings using polydimethylsiloxane (PDMS) as an adhesive. Both micro-ECoG devices and steel-backed intracortical array devices were inserted into zero-insertion force (ZIF) connectors on custom printed circuit boards for connection to the data acquisition systems for *in vitro* characterization or *in vivo* neural recording.

Author Manuscript Author Manuscript Author Manuscript Author Manuscript

Author Manuscript Author Manuscript Author Manuscript Author Manuscript

Electrochemical Impedance Spectroscopy.

EIS of Ti_3C_2 and Au microelectrodes was performed with a Gamry Reference 600 potentiostat (Gamry Instruments) in a phosphate-buffered saline (PBS) bath of pH 7.4 at room temperature. EIS measurements were collected using a three-electrode configuration with Ti_3C_2 or Au microelectrodes as the working electrode, a graphite rod (Bio-Rad Laboratories, Inc.) as the counter electrode, and a Ag/AgCl (Sigma-Aldrich) electrode as the reference electrode. Measurements were acquired by applying a 20 mV rms sinusoidal voltage input in the 1 Hz–1 MHz range.

Electrode Surface Morphology Characterization.

SEM images (Zeiss Supra 50VP) were taken with an accelerating voltage of 5 kV. AFM surface mapping (Bruker Dimension Icon AFM) was performed in tapping mode in air, and data were analyzed in NanoScope Analysis software (Bruker).

Animal Surgery and *In Vivo* Recording.

In vivo neural recordings were collected from $n = 3$ Sprague Dawley rats during acute, sterile procedures. Rats were anesthetized with a solution of ketamine (60 mg/kg) and dexmedetomidine (0.25 mg/kg) and placed in a stereotaxic frame. The right somatosensory cortex was exposed with a craniectomy and durotomy. Skull screws were placed in the left parietal and frontal bones around which Ag wires were wrapped to serve as the reference and ground for the recordings. The electrode arrays were mounted on a stereotaxic manipulator, positioned over the exposed cortex, and lowered. Ti_3C_2 and Au micro-ECoG arrays were placed over barrel cortex successively, and recordings from each were collected in 5 min segments. For intracortical Ti_3C_2/Au arrays, recordings were made at a number of depths throughout the cortex to sample neural activity. The wideband neural signals (1 Hz to 7.5 kHz) were acquired at 30 000 samples per second by an electrophysiology system (Intan RHS2000 Stimulation/Recording System, Intan Technologies). All procedures were approved by the Institutional Animal Care and Use Committees at the University of Pennsylvania and adhered to the guidelines set forth in the NIH Public Health Service Policy on Humane Care and Use of Laboratory Animals (2015).

In Vivo Data Analysis and Statistical Methods.

For multiunit analysis, signals were band-pass filtered from 300 to 6000 Hz (2nd order Butterworth). The standard deviation of the background noise for each channel was estimated as:

$$\sigma_n = \text{median}\left\{\frac{|x|}{0.6745}\right\}$$

and spikes were detected by setting a threshold of $5\sigma n$. Spikes observed on both the Ti_3C_2 and Au electrode in a stereotrode pair were assumed to have been generated by the same neuron, and thus classified as “common spikes”, if they occurred within 0.1 ms of each other. All remaining spikes were classified as “unique spikes”. To ompare signal quality, the SNRs for each common spike were computed from the signals observed on the Ti_3C_2 and

Author Manuscript

Author Manuscript

Author Manuscript

Author Manuscript

Au electrodes in the stereotrode pair and subtracted. A permutation test was then performed to test if the mean of the resulting distribution was centered around 0.

Cell-Culture Substrate Preparation.

Glass slides coated with Ti_3C_2 were soaked in 70% ethanol for 20 min. Slides were then rinsed in sterile cell-culture water before exposing each side to UV light for 30 min (1 h total exposure). After UV treatment, slides were immersed in poly-L-lysine (PLL) (0.05 mg/mL in sterile cell culture water) overnight. Slides were then rinsed in sterile cell-culture water before being immersed in laminin (20 μg/mL in sterile cell-culture water) overnight prior to neuronal plating. For control cultures, polystyrene Petri dishes were coated in PLL and laminin using the same protocol.

Cortical Neuron Isolation and Culture.

All procedures were approved by the Institutional Animal Care and Use Committees at the University of Pennsylvania and the Michael J. Crescenz Veterans Affairs Medical Center and adhered to the guidelines set forth in the NIH Public Health Service Policy on Humane Care and Use of Laboratory Animals (2015). Neural cell isolation and culture were performed following protocols previously published. Briefly, rats with a predetermined mating schedule were euthanized, and embryonic day 18 fetuses were removed from the uterus and transferred to cold Hank's balanced salt solution (HBSS). After removal, the fetus brains were extracted and the cerebral cortical hemispheres isolated under a stereoscope via microdissection. Cortical tissue was dissociated in 0.25% trypsin and1 mM Ethyl-enediaminetetraacetic acid (EDTA) at 37 °C, after which the trypsin/EDTA mixture was removed and replaced with 0.15 mg/mL DNase in HBSS. Dissociated tissue and DNase was centrifuged for 3 min at 3000 rpm before the DNase was removed and the cells resuspended in neuronal culture media, composed of Neurobasal plus B27 and Glutamax (ThermoFisher) and 1% penicillin–streptomycin. Neurons were diluted to $\sim 1.5 \times 10^6$ neurons per milliliter. A total of 200 μL from the primary cortical neuronal suspensions was plated on each of the Ti_3C_2 slides and control dishes within 2 mL of neuronal culture media and grown under standard cell culture conditions (37 °C, 5% CO_2). Half-media changes were performed every 2 days, with phase images taken using a Nikon Eclipse Ti–S microscope paired with a QIClick camera and NIS Elements BR 4.13.00.

Neuronal Viability Assessment.

To assess culture viability, phase images of Ti_3C_2 slides ($n = 6$) and control cultures ($n = 6$) were taken at 7 days *in vitro* (DIV). Neurons within a randomly identified 0.5 mm^2 area were manually scored as either live or dead depending on their morphology (*i.e.*, presence and integrity of neurites and cell body). Neuronal survival was quantified as the proportion of live neurons to total (live and dead) neurons, while cell density was calculated as the total number of neurons per square millimeter. Each metric was averaged across Ti_3C_2 and polystyrene controls and compared via unpaired t test, with statistical significance identified as a p value of less than 0.05. All data were presented as mean plus or minus the standard error of the mean.

Author Manuscript Author Manuscript Author Manuscript Author Manuscript

Immunocytochemistry.

At 7 DIV, Ti_3C_2 slides ($n = 6$) and control cultures (n = 6) were fixed in 4% formaldehyde for 35 min. Fixed cultures were rinsed in 1× PBS and permeabilized with 0.3% Triton ×100 and 4% horse serum in PBS for 60 min before being incubated with primary antibodies overnight at 4 °C. Primary antibodies were Tuj-1/β-III tubulin (T8578, 1:500, Sigma-Aldrich) to label axons and synapsin-1 (A6442, 1:500, Invitrogen) to label presynaptic specializations. Post-incubation, cultures were rinsed in PBS before being incubated with fluorescently labeled secondary antibodies (1:500; sourced from Life Technologies and Invitrogen) for 2 h at 18°−24 °C. Finally, Hoechst (33342, 1:10 000, ThermoFisher) was added for 10 min at 18°−24 °C before rinsing in PBS. Cultures were imaged on a Nikon A1RMP+ multiphoton confocal microscope paired with NIS Elements AR 4.60.00 and a 16× immersion objective. Sequential slices of 1–1.2 μm in the z plane ($n_{\text{slices}} = 20$) were acquired for each fluorescent channel. All confocal images presented are maximum intensity projections of the confocal z slices.

Neurite Measurement and Data Analysis.

Multiphoton images from the immunocytochemistry performed above were imported into ImageJ and processed using the open-source NeuriteQuant plugin. NeuriteQuant provided quantitative estimates of neurites per cell from the multiphoton images. Neurites per cell were averaged for both polystyrene and Ti_3C_2 cultures, with unpaired t tests being used to compare measurements. All data are presented as mean plus or minus the standard error of the mean.

Supplementary Material

Refer to Web version on PubMed Central for supplementary material.

ACKNOWLEDGMENTS

This work was supported by the National Institutes of Health (grant no. U01-NS094340 to D.K.C.); Department of Veterans Affairs (BLR&D Merit Review no. I01-BX003748 to D.K.C.); Citizens United for Research in Epilepsy Taking Flight Award (F.V.); Mirowski Family Foundation, and Neil and Barbara Smit (F.V.); National Science Foundation Graduate Research Fellowship Program (grant no. DGE 1321851 to N.D.); and the NNCI Mid-Atlantic Nanotechnology Hub (MANTH) for Research, Education, & Innovation (NSF award no. 1542153 to L.E.). Any opinions, findings, and conclusions or recommendations expressed in this material are those of the author(s) and do not necessarily reflect the views of the National Institutes of Health, Department of Veterans Affairs, or the National Science Foundation. The funders had no role in the study design, data collection and analysis, decision to publish, or preparation of the manuscript.

REFERENCES

(1). Polikov VS; Tresco PA; Reichert WM Response of Brain Tissue to Chronically Implanted Neural Electrodes. J. Neurosci. Methods 2005, 148, 1–18. [PubMed: 16198003]

(2). Ferguson JE; Boldt C; Redish AD Creating Low-Impedance Tetrodes by Electroplating with Additives. Sens. Actuators, A 2009, 156, 388–393.

(3). Boehler C; Stieglitz T; Asplund M. Nanostructured Platinum Grass Enables Superior Impedance Reduction for Neural Microelectrodes. Biomaterials 2015, 67, 346–353. [PubMed: 26232883]

(4). Petrossians A; Whalen JJ; Weiland JD; Mansfeld F. Surface Modification of Neural Stimulating/Recording Electrodes with High Surface Area Platinum-Iridium Alloy Coatings. In 2011 Annual

Author Manuscript Author Manuscript Author Manuscript Author Manuscript

International Conference of the IEEE Engineering in Medicine and Biology Society; IEEE: Piscataway, NJ, 2011; pp 3001–3004.

(5). Meyer RD; Cogan SF; Nguyen TH; Rauh RD Electrodeposited Iridium Oxide for Neural Stimulation and Recording Electrodes. IEEE Trans. Neural Syst. Rehabil. Eng. 2001, 9, 2–11. [PubMed: 11482359]

(6). Lu Y; Lyu H; Richardson AG; Lucas TH; Kuzum D. Flexible Neural Electrode Array Based-on Porous Graphene for Cortical Microstimulation and Sensing. Sci. Rep 2016, 6, 33526. [PubMed: 27642117]

(7). Keefer EW; Botterman BR; Romero MI; Rossi AF; Gross GW Carbon Nanotube Coating Improves Neuronal Recordings. Nat. Nanotechnol 2008, 3, 434–439. [PubMed: 18654569]

(8). Vitale F; Summerson SR; Aazhang B; Kemere C; Pasquali M. Neural Stimulation and Recording with Bidirectional, Soft Carbon Nanotube Fiber Microelectrodes. ACS Nano 2015, 9, 4465–4474. [PubMed: 25803728]

(9). Patolsky F; Timko BP; Yu G; Fang Y; Greytak AB; Zheng G; Lieber CM Detection, Stimulation, and Inhibition of Neuronal Signals with High-Density Nanowire Transistor Arrays. Science 2006, 313, 1100–1104. [PubMed: 16931757]

(10). Kotov NA; Winter JO; Clements IP; Jan E; Timko BP; Campidelli S; Pathak S; Mazzatenta A; Lieber CM; Prato M; Bellamkonda RV; Silva GA; Kam NWS; Patolsky F; Ballerini L. Nanomaterials for Neural Interfaces. Adv. Mater 2009, 21, 3970–4004.

(11). Matarredona O; Rhoads H; Li Z; Harwell JH; Balzano L; Resasco DE Dispersion of Single-Walled Carbon Nanotubes in Aqueous Solutions of the Anionic Surfactant NaDDBS. J. Phys. Chem. B 2003, 107, 13357–13367.

(12). Ramesh S; Ericson LM; Davis VA; Saini RK; Kittrell C; Pasquali M; Billups WE; Adams WW; Hauge RH; Smalley RE Dissolution of Pristine Single Walled Carbon Nanotubes in Superacids by Direct Protonation. J. Phys. Chem. B 2004, 108, 8794–8798.

(13). Kim SW; Kim T; Kim YS; Choi HS; Lim HJ; Yang SJ; Park CR Surface Modifications for the Effective Dispersion of Carbon Nanotubes in Solvents and Polymers. Carbon 2012, 50, 3–33.

(14). Wang J; Sun J; Gao L; Wang Y; Zhang J; Kajiura H; Li Y; Noda K. Removal of the Residual Surfactants in Transparent and Conductive Single-Walled Carbon Nanotube Films. J. Phys. Chem. C 2009, 113, 17685–17690.

(15). Hecht DS; Heintz AM; Lee R; Hu L; Moore B; Cucksey C; Risser S. High Conductivity Transparent Carbon Nanotube Films Deposited from Superacid. Nanotechnology 2011, 22, 169501.

(16). Wang M; Mi G; Shi D; Bassous N; Hickey D; Webster TJ Nanotechnology and Nanomaterials for Improving Neural Interfaces. Adv. Funct. Mater 2018, 28, 1700905.

(17). Li X; Zhu Y; Cai W; Borysiak M; Han B; Chen D; Piner RD; Colombo L; Ruoff RS Transfer of Large-Area Graphene Films for High-Performance Transparent Conductive Electrodes. Nano Lett 2009, 9, 4359–4363. [PubMed: 19845330]

(18). Anasori B; Lukatskaya M; Gogotsi Y. 2D Metal Carbides and Nitrides (MXenes) for Energy Storage. Nat. Rev. Mats 2017, 2, 16098.

(19). Lukatskaya MR; Kota S; Lin Z; Zhao M-Q; Shpigel N; Levi MD; Halim J; Taberna P-L; Barsoum MW; Simon P; Gogotsi Y Ultra-High-Rate Pseudocapacitive Energy Storage in Two-Dimensional Transition Metal Carbides. Nature Energy. 2017, 2, 17105.

(20). Rakhi RB; Nayak P; Xia C; Alshareef HN Novel Amperometric Glucose Biosensor Based on MXene Nanocomposite. Sci. Rep 2016, 6, 36422. [PubMed: 27830757]

(21). Kim SJ; Koh H-J; Ren CE; Kwon O; Maleski K; Cho S-Y; Anasori B; Kim C-K; Choi Y-K; Kim J; Gogotsi Y; Jung H-T Metallic $Ti_3C_2T_x$ MXene Gas Sensors with Ultrahigh Signal-to-Noise Ratio. ACS Nano 2018, 12, 986–993. [PubMed: 29368519]

(22). Chen X; Sun X; Xu W; Pan G; Zhou D; Zhu J; Wang H; Bai X; Dong B; Song H. Ratiometric Photoluminescence Sensing Based on Ti_3C_2 MXene Quantum Dots as an Intracellular PH Sensor. Nanoscale 2018, 10, 1111–1118. [PubMed: 29271463]

(23). Lin H; Wang Y; Gao S; Chen Y; Shi J. Theranostic 2D Tantalum Carbide (MXene). Adv. Mater 2018, 30, 1703284.

Author Manuscript Author Manuscript Author Manuscript Author Manuscript

(24). Xuan J; Wang Z; Chen Y; Liang D; Cheng L; Yang X; Liu Z; Ma R; Sasaki T; Geng F. Organic-Base-Driven Intercalation and Delamination for the Production of Functionalized Titanium Carbide Nanosheets with Superior Photothermal Therapeutic Performance. Angew. Chem., Int. Ed 2016, 55, 14569–14574.

(25). Xu B; Zhu M; Zhang W; Zhen X; Pei Z; Xue Q; Zhi C; Shi P. Ultrathin MXene-Micropattern-Based Field-Effect Transistor for Probing Neural Activity. Adv. Mater 2016, 28, 3333–3339. [PubMed: 26924616]

(26). Naguib M; Kurtoglu M; Presser V; Lu J; Niu J; Heon M; Hultman L; Gogotsi Y; Barsoum MW Two-Dimensional Nanocrystals Produced by Exfoliation of Ti_3AlC_2. Adv. Mater 2011, 23, 4248–4253. [PubMed: 21861270]

(27). Alhabeb M; Maleski K; Anasori B; Lelyukh P; Clark L; Sin S; Gogotsi Y. Guidelines for Synthesis and Processing of Two-Dimensional Titanium Carbide ($Ti_3C_2T_x$ MXene). Chem. Mater 2017, 29, 7633–7644.

(28). Ghidiu M; Lukatskaya MR; Zhao M-Q; Gogotsi Y; Barsoum MW Conductive Two-Dimensional Titanium Carbide ‘Clay’ with High Volumetric Capacitance. Nature 2014, 516, 78–81. [PubMed: 25470044]

(29). Zhang CJ; Anasori B; Seral-Ascaso A; Park S-H; McEvoy N; Shmeliov A; Duesberg GS; Coleman JN; Gogotsi Y; Nicolosi V. Transparent, Flexible, and Conductive 2D Titanium Carbide (MXene) Films with High Volumetric Capacitance. Adv. Mater 2017, 29, 1702678.

(30). Zhu Y; Murali S; Stoller MD; Ganesh KJ; Cai W; Ferreira PJ; Pirkle A; Wallace RM; Cychosz KA; Thommes M; Su D; Stach EA; Ruoff RS Carbon-Based Supercapacitors Produced by Activation of Graphene. Science 2011, 332, 1537–1541. [PubMed: 21566159]

(31). Heon M; Lofland S; Applegate J; Nolte R; Cortes E; Hettinger JD; Taberna P-L; Simon P; Huang P; Brunet M; Gogotsi Y. Continuous Carbide-Derived Carbon Films with High Volumetric Capacitance. Energy Environ. Sci 2011, 4, 135–138.

(32). Yang X; Cheng C; Wang Y; Qiu L; Li D. Liquid-Mediated Dense Integration of Graphene Materials for Compact Capacitive Energy Storage. Science 2013, 341, 534–537. [PubMed: 23908233]

(33). McNaughton BL; O’Keefe J; Barnes CA The Stereotrode: A New Technique for Simultaneous Isolation of Several Single Units in the Central Nervous System from Multiple Unit Records. J. Neurosci. Methods 1983, 8, 391–397. [PubMed: 6621101]

(34). Sessolo M; Khodagholy D; Rivnay J; Maddalena F; Gleyzes M; Steidl E; Buisson B; Malliaras GG Easy-to-Fabricate Conducting Polymer Microelectrode Arrays. Adv. Mater 2013, 25, 2135–2139. [PubMed: 23417987]

(35). Dall’Agnese Y; Lukatskaya MR; Cook KM; Taberna P-L; Gogotsi Y; Simon P. High Capacitance of Surface-Modified 2D Titanium Carbide in Acidic Electrolyte. Electrochem. Commun 2014, 48, 118–122.

(36). Levi MD; Lukatskaya MR; Sigalov S; Beidaghi M; Shpigel N; Daikhin L; Aurbach D; Barsoum MW; Gogotsi Y. Solving the Capacitive Paradox of 2D MXene Using Electrochemical Quartz-Crystal Admittance and *In Situ* Electronic Conductance Measurements. Adv. Energy Mater 2015, 5, 1400815.

(37). Richardson AG; Liu X; Weigand PK; Hudgins ED; Stein JM; Das SR; Proekt A; Kelz MB; Zhang M; Van der Spiegel J; Lucas TH Hippocampal Gamma-Slow Oscillation Coupling in Macaques during Sedation and Sleep. Hippocampus 2017, 27, 1125–1139. [PubMed: 28667703]

(38). Pal D; Silverstein BH; Sharba L; Li D; Hambrecht-Wiedbusch VS; Hudetz AG; Mashour GA Propofol, Sevoflurane, and Ketamine Induce a Reversible Increase in Delta-Gamma and Theta-Gamma Phase-Amplitude Coupling in Frontal Cortex of Rat. Front. Syst. Neurosci 2017, 11, 41. [PubMed: 28659769]

(39). Dai C; Chen Y; Jing X; Xiang L; Yang D; Lin H; Liu Z; Han X; Wu R. Two-Dimensional Tantalum Carbide (MXenes) Composite Nanosheets for Multiple Imaging-Guided Photothermal Tumor Ablation. ACS Nano 2017, 11, 12696–12712. [PubMed: 29156126]

(40). Rakhi RB; Nayak P; Xia C; Alshareef HN Novel Amperometric Glucose Biosensor Based on MXene Nanocomposite. Sci. Rep 2016, 6, 36422. [PubMed: 27830757]

Author Manuscript Author Manuscript Author Manuscript Author Manuscript

(41). Han X; Huang J; Lin H; Wang Z; Li P; Chen Y. 2D Ultrathin MXene-Based Drug-Delivery Nanoplatform for Synergistic Photothermal Ablation and Chemotherapy of Cancer. Adv. Healthcare Mater 2018, 7, 1701394.

(42). Dai C; Lin H; Xu G; Liu Z; Wu R; Chen Y. Biocompatible 2D Titanium Carbide (MXenes) Composite Nanosheets for PH-Responsive MRI-Guided Tumor Hyperthermia. Chem. Mater 2017, 29, 8637–8652.

(43). Quiroga RQ; Nadasdy Z; Ben-Shaul Y. Unsupervised Spike Detection and Sorting with Wavelets and Superparamagnetic Clustering. Neural Comput 2004, 16, 1661–1687. [PubMed: 15228749]

(44). Harris JP; Struzyna LA; Murphy PL; Adewole DO; Kuo E; Cullen DK Advanced Biomaterial Strategies to Transplant Preformed Micro-Tissue Engineered Neural Networks into the Brain. J. Neural Eng 2016, 13, 016019. [PubMed: 26760138]

Author Manuscript

Author Manuscript

Author Manuscript

Author Manuscript

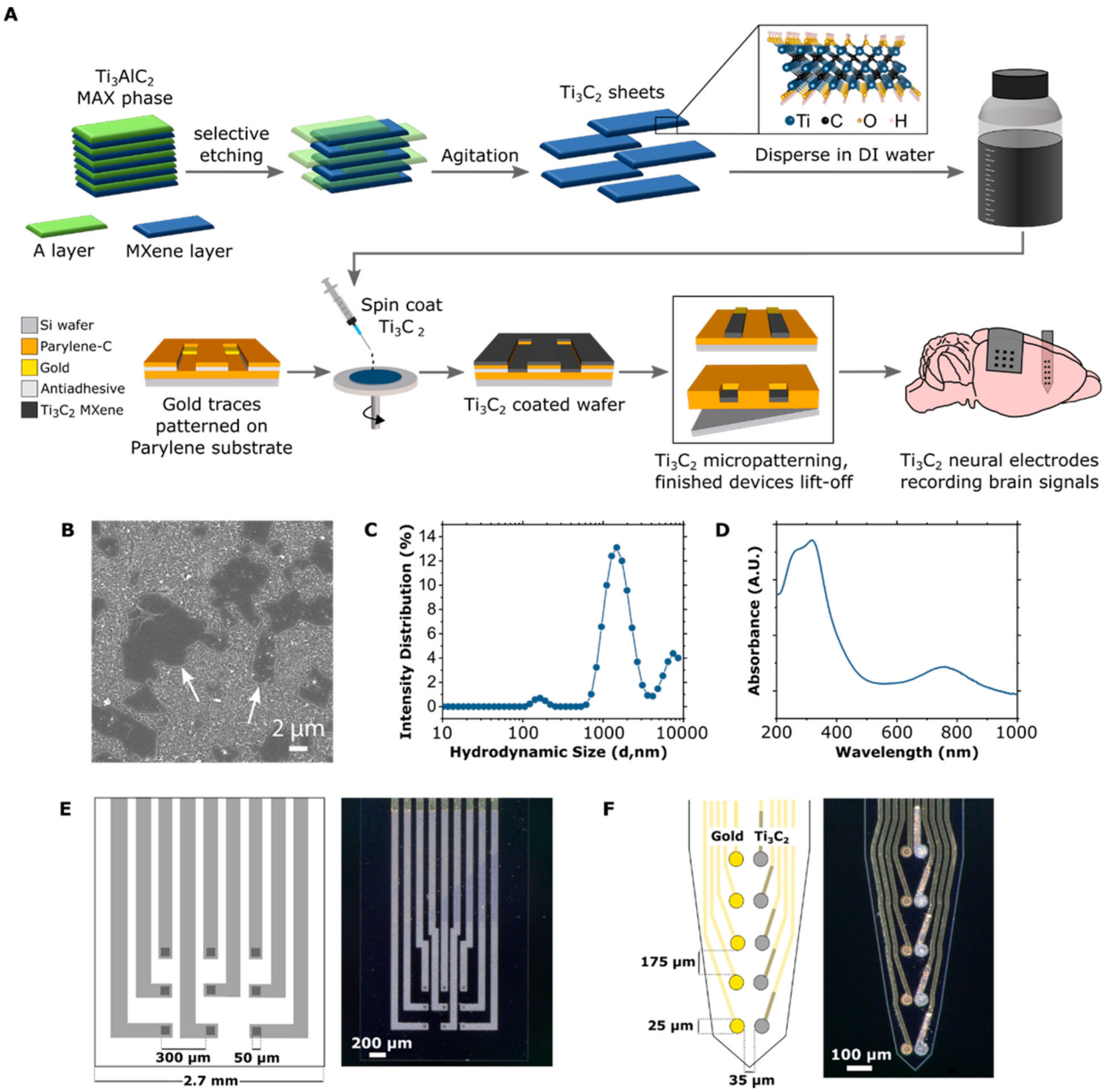

Figure 1.

Synthesis, characterization, and application of Ti_3C_2 for neural recording. (A) Schematics illustrating synthesis and atomic structure of Ti_3C_2, fabrication of Ti_3C_2 neural microelectrode arrays, and application of Ti_3C_2 arrays for recording brain activity at different locations in the rat brain. (B) SEM image of Ti_3C_2 flakes deposited onto an alumina membrane. The arrows point to Ti_3C_2 flakes on the membrane. (C) Dynamic light scattering particle size intensity distribution (percent) of the Ti_3C_2 solution in terms of hydrodynamic size (d, nanometer) (D) UV–vis absorption spectra of the Ti_3C_2 aqueous solution diluted 1000×. (E, F) Schematics and bright-field microscopy image of (E) Ti_3C_2 micro-ECoG array and (F) Ti_3C_2/Au intracortical electrode array.

Author Manuscript
Author Manuscript
Author Manuscript
Author Manuscript

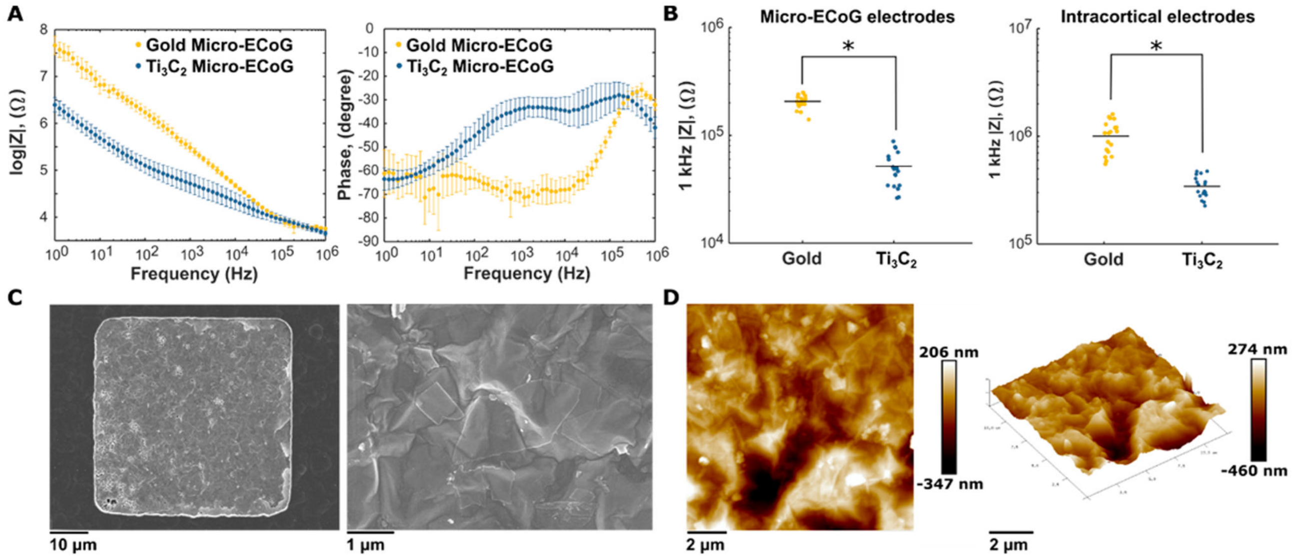

Figure 2.

Characterization of Ti_3C_2 neural electrodes. (A) Bode plots of impedance magnitude and phase for comparable Ti_3C_2 and Au micro-ECoG electrodes. Points represent means, and bars show standard deviations; Ti_3C_2 $n = 10$ and Au $n = 10$. (B) Scatter plots of 1 kHz impedance values for Ti_3C_2 and Au electrodes in micro-ECoG and intracortical electrode arrays. Micro-ECoG electrodes are 50 μm × 50 μm, and intracortical electrodes are 25 μm in diameter. For both types of electrode arrays, Ti_3C_2 shows an ~4× reduction in impedance compared to Au. Black bars indicate means. Micro-ECoG: Ti_3C_2 n =18 and Au $n = 18$. Intracortical: Ti_3C_2 $n = 19$ and Au $n = 19$. Single asterisks indicate $p < 0.001$ (C) SEM images of Ti_3C_2 electrodes. Individual Ti_3C_2 flakes are visible on the electrode surface. (D) AFM surface mapping showing the rough surface morphology of a Ti_3C_2 electrode.

Author Manuscript
Author Manuscript
Author Manuscript
Author Manuscript

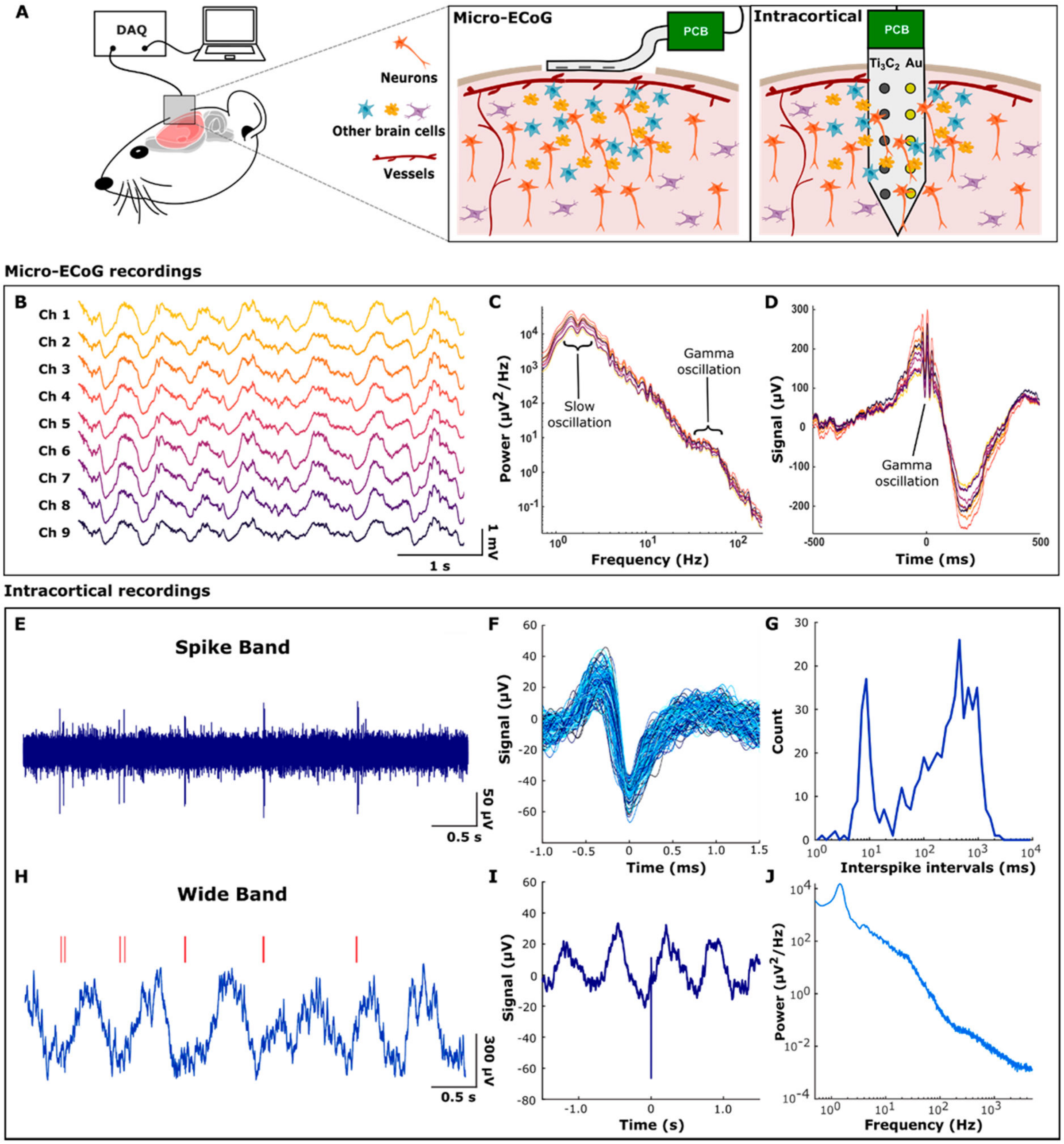

Figure 3.

In vivo neural recordings with Ti_3C_2 MXene electrodes. (A) Schematic of in vivo neural recording with Ti_3C_2 electrode arrays. Ti_3C_2 micro-ECoG arrays were placed on the cortical surface after craniotomies were performed, and Ti_3C_2/Au intracortical arrays were inserted into the cortex through a burr hole. Devices were connected via a custom printed circuit board to the data-acquisition system. (B) Raw signals obtained from a Ti_3C_2 micro-ECoG device. (C) Power spectral density of micro-ECoG signals showing physiologic peaks for 1–2 Hz slow oscillations and 40–70 Hz γ oscillations. (D) The γ-triggered average showing γ oscillations coupled to the up phase of the slow oscillation. (E) Action potentials (spikes)

Author Manuscript

Author Manuscript

Author Manuscript

Author Manuscript

recorded extracellularly in rat hippocampus under ketamine–dexmedetomidine anesthesia. Noise in the spike frequency band (500–5000 Hz) was 4.67 μVrms. (F) Overlaid spike waveforms ($N = 580$) from a 200 s recording. (G) Interspike intervals had a bimodal distribution. The neuron tended to fire rhythmically at 1 to 2 Hz with bursts of 2 spikes separated by about 10 ms. (H) The full bandwidth (0.5–5000 Hz) recording revealed that the rhythmic spiking was related to a slow oscillation in the field potential. Red lines indicate spike times corresponding to E. (I) Spike-triggered average showing that the spikes were locked to the rising phase of the slow oscillation. (J) Power spectrum of the full bandwidth recording with a physiological peak at 1.5 Hz.

Author Manuscript

Author Manuscript

Author Manuscript

Author Manuscript

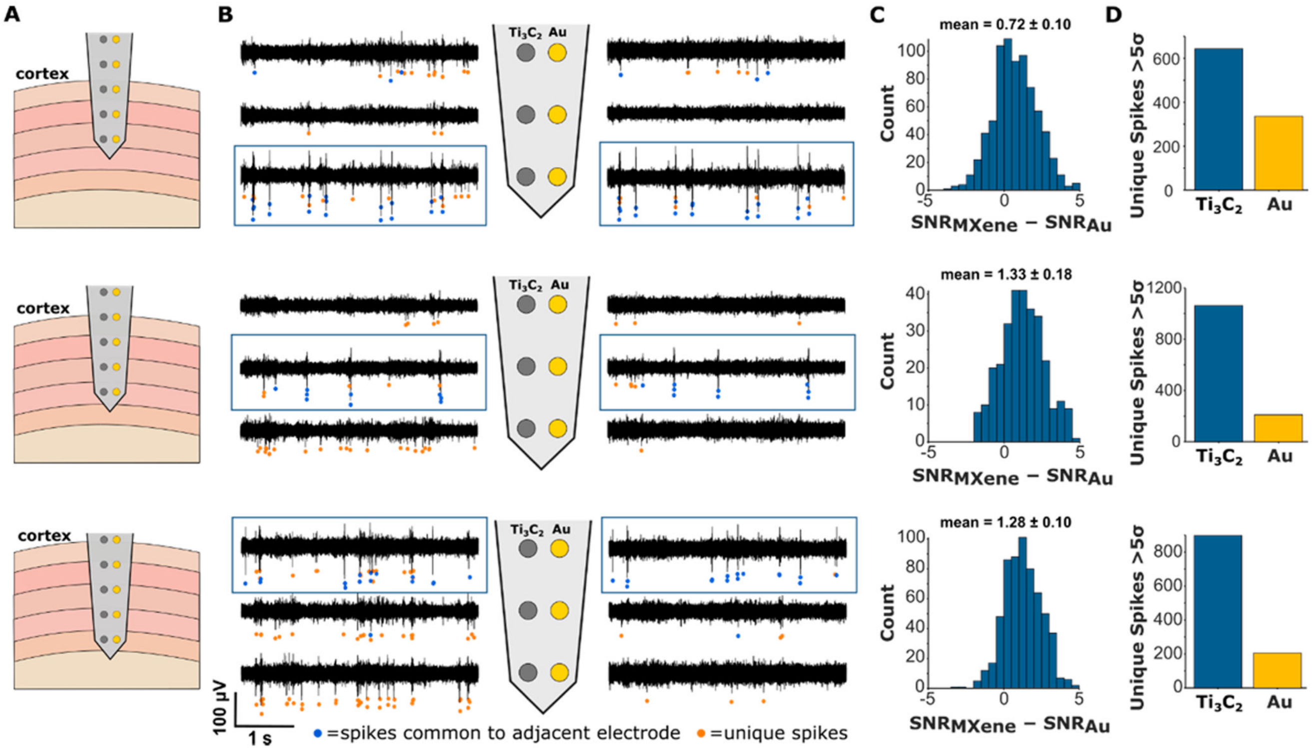

Figure 4.

Comparison of *in vivo* signal recorded on Ti_3C_2 and Au electrodes intracortically. (A) Schematics of an intracortical electrode array with five Ti_3C_2–Au stereotrode pairs. The array was inserted into the cortex and advanced in approximately 500 μm steps to a depth of 2 mm while recording. (B) Multi-unit spiking activity observed on the distal three pairs of electrodes in the array at three different recording depths. Spikes that were observed simultaneously on adjacent Ti_3C_2 and Au contacts are indicated by blue dots. Spikes unique to a given electrode are indicated by orange dots. (C) Histogram of SNR_{MXene}–SNR_{Au} for the common spikes on the adjacent electrodes outlined in blue boxes in panel B. In all cases, the distribution mean was significantly greater than zero (permutation tests, $p < 0.001$), indicating higher SNR on Ti_3C_2 contacts compared to Au. (D) Number of unique spikes seen on adjacent Ti_3C_2 and Au electrodes. In all cases, more unique spikes were observed on Ti_3C_2 contacts, indicating that these electrodes were more sensitive for recording unit activity than Au electrodes.

Author Manuscript

Author Manuscript

Author Manuscript

Author Manuscript

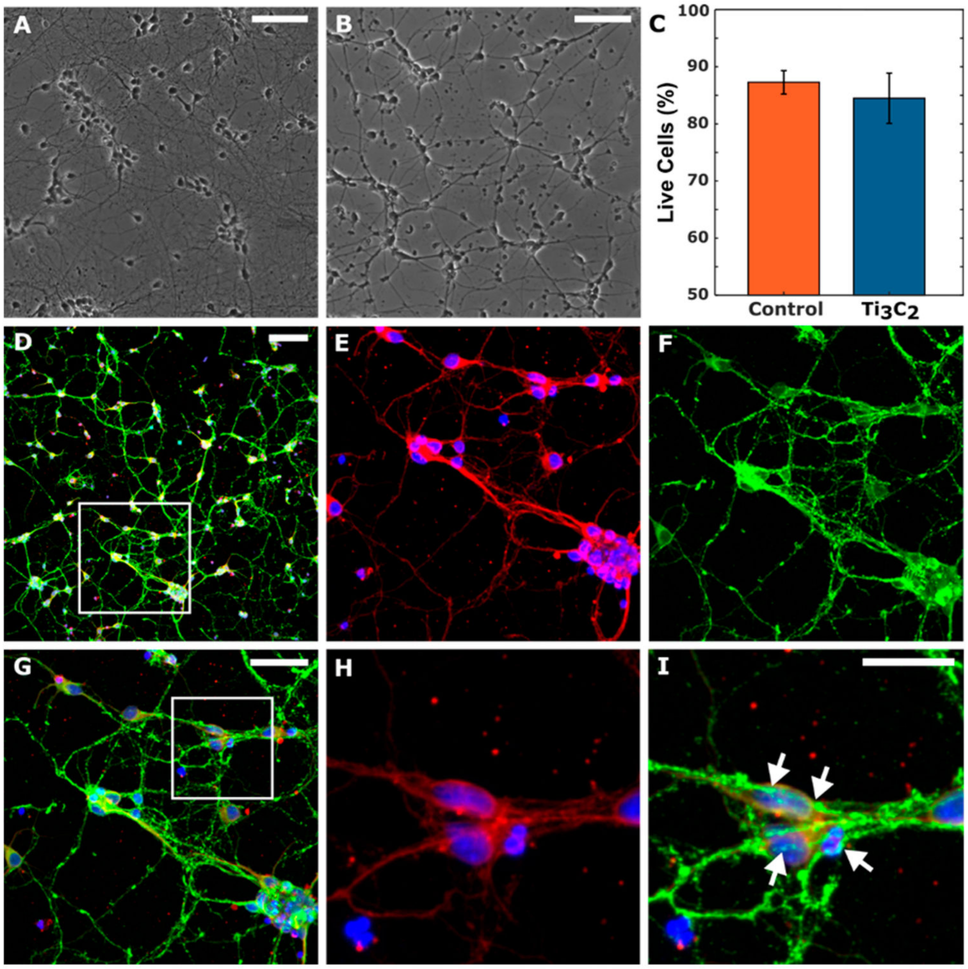

Figure 5.

Biocompatibility of Ti_3C_2 MXene films. Representative phase images of primary cortical neurons cultured on (A) polystyrene and (B) 200 nm thick Ti_3C_2 films at 7 DIV. (C) Quantitative comparison shows no significant difference in neuronal survival on Ti_3C_2 or polystyrene ($p > 0.6$). (D–I) Representative multiphoton images of neurons cultured on Ti_3C_2 at 7 DIV stained for nuclei (blue), axons (red), and synapses (green). Outlined region in panel D is shown in panels E–G; the outlined region in panel G is shown in panels H and I, highlighting the network formation as confirmed by the presence of synapsin-positive puncta along the axons and cell bodies (arrows). Scale bars: 100 μm (panels A, B, and D), 50 μm (panel G), 25 μm (panel I).